DENSE CELL-BY-CELL SYSTEMS OF PDES: APPROXIMATION, SPECTRAL ANALYSIS, AND PRECONDITIONING*

PIETRO BENEDUSI†, PAOLA FERRARI‡, MARIUS CAUSEMANN§, AND STEFANO SERRA-CAPIZZANO¶

Abstract. In the present study, we consider the Extra-Membrane-Intra model (EMI) for the simulation of excitable tissues at the cellular level. We provide the (possibly large) system of partial differential equations (PDEs), equipped with ad hoc boundary conditions, relevant to model portions of excitable tissues, composed of several cells. In particular, we study two geometrical settings: computational cardiology and neuroscience. The Galerkin approximations to the considered system of PDEs lead to large linear systems of algebraic equations, where the coefficient matrices depend on the number N of cells and the fineness parameters. We give a structural and spectral analysis of the related matrix-sequences with N fixed and with fineness parameters tending to zero. Based on the theoretical results, we propose preconditioners and specific multilevel solvers. Numerical experiments are presented and critically discussed, showing that a monolithic multilevel solver is efficient and robust with respect to all the problem and discretization parameters. In particular, we include numerical results increasing the number of cells N, both for idealized geometries (with N exceeding 10^5) and for realistic, densely populated 3D tissue reconstruction.

Key words. spectral distribution, symbol, preconditioning, iterative solvers, cell-by-cell, EMI, electrophysiology

MSC codes. 15A18, 35Q92, 65F08, 65F50, 65N55, 65N30

1. Introduction. The cell-by-cell framework, also known as EMI (Extra, Intra, Membrane) model, is a successful tool in computational electrophysiology, employed to simulate excitable tissues at a cellular scale. Compared to homogenized models, such as the well-known mono- and bidomain equations, its essential novelty consists in resolving cell morphologies explicitly, enabling detailed biological simulations. In contrast, homogenized models assume extra- and intracellular quantities to be defined in the whole spatial domain without a geometrical representation of cell membranes. In this sense, EMI models allow a more detailed modelling of cellular interplay, for example resolving complex cell networks or capturing inhomogeneities along cells membranes. The interested reader is referred to [46], where an exhaustive description of the EMI model, its derivation, some theoretical results, and several applications are presented and discussed in detail. This framework is especially well suited to simulate cellular activity in the human brain, where the cell-scale morphology is highly complex [7, 19]. In this context, 3D dense reconstructions of neural tissue have recently become available [48, 36, 41, 13, 6]. Moreover, in the field of computational cardiology, we see a growing interest in modeling cardiomyocytes, with their structured pattern [38, 28, 30, 29, 45]. In both applications, it is essential to accurately resolve the propagation of electrical excitation in the tissue under examination [12, 20, 21, 14, 35].

Considering the realistic setting of a tissue composed of several cells, with possibly different properties, we provide the associated system of partial differential equations (PDEs) coupled via membrane ordinary differential equations ODEs, and equipped

†Euler Institute, Università della Svizzera Italiana, Lugano, Switzerland (benedp@usi.ch).
‡Department of Mathematics, University of Genoa, Genoa, Italy
School of Mathematics and Natural Sciences, University of Wuppertal, Wuppertal, Germany
§Simula Research Laboratory, Oslo, Norway
¶University of Insubria, Como, Italy
Uppsala University, Uppsala, Sweden

with ad hoc boundary conditions. Subsequently, we consider Galerkin-type approximations of the PDEs system, leading to large linear systems of algebraic equations, where the resulting coefficient matrices depend on the number N of cells and on the spatial discretization. The resulting matrices present different levels of structure: at the outermost level, we have a block structure (e.g. a block arrowhead structure in the context of neuroscience applications), while each block has a (block) two-level Toeplitz [47, 44] or (block) two-level Generalized Locally Toeplitz (GLT) nature [25, 4]. The number of levels is dictated by the dimensionality of the domain. For example, in the case of three-dimensional domains a (block) three-level Toeplitz or (block) three-level GLT (asymptotical) structure would occur in any single block.

By generalizing the work in [9], concerning the case of $N = 1$, our study is developed in the following two directions:

(i) first we give a structural and spectral analysis of the EMI matrix-sequences with N fixed and with fineness parameters tending to zero;

(ii) based on the the theoretical results, we propose preconditioners and specific multilevel solvers, tested in different application settings, both for idealized and realistic geometries, varying the number of cells N and discretization parameters.

We emphasize that the GLT analysis is not completely sufficient for the considered setting and hence specific theoretical tools are developed here, allowing us to give a quite complete picture of the spectral features of the resulting matrices and matrix-sequences (e.g. the eigenvalue distribution). Numerical experiments are presented and critically discussed, showing the efficiency and robustness of a proposed monolithic multilevel strategy. As a benchmark, we highlight [30], where an efficient solution strategy is described for an idealized cardiac geometry, discretized with finite differences, increasing the number of cells up to $N > 10^5$.

The present work is organized as follows. In Section 2 the continuous problem is introduced together with possible generalizations. Section 3 considers a basic Galerkin strategy for approximating the examined problem. The spectral analysis is given in Section 4 in terms of distribution results and degenerating eigenspaces. Specifically, Subsection 4.1 lays out the foundational theories and concepts necessary to understand the distribution of the entire system (presented in a general form in Subsection 4.2) and the specific stiffness matrices and matrix-sequences (discussed in Subsection 4.3). These findings represent the starting point for proposing in Section 5 a preconditioned multilevel strategy, where a selection of numerical experiments is discussed, in connection with the spectral analysis and the related algorithmic proposals. Finally, Section 6 contains conclusions and a list of relevant open problems.

2. The EMI model. We introduce the partial differential equations characterizing the EMI model. Compared to homogenized models, we observe that the novelty of the EMI approach lies in the fact that the cellular membrane Γ is explicitly represented, as well as the intra- and extra-cellular subdomains.

We consider a domain $\Omega \subset \mathbb{R}^d$, with typically $d \in \{2,3\}$, composed of N disjoint domains, or cells, $\Omega_1, \Omega_2, \ldots, \Omega_N$, an extracellular media Ω_0 surrounding the N cells, so that $\overline{\Omega} = \bigcup_{i=0}^{N} \overline{\Omega}_i$. We define cell membranes $\Gamma_i = \partial\Omega_i/\partial\Omega$ for $i = 0, \ldots, N$ and the full membrane $\Gamma = \bigcup_{i=0}^{N} \Gamma_i$. Moreover, we define possible common interfaces, as $\Gamma_{ij} = \partial\Omega_i \cap \partial\Omega_j$, for $i, j = 0, \ldots, N$ and $i \neq j$, satisfying $\Gamma_{ij} \subseteq \Gamma_i$. We refer to Fig. 1 for an example of this geometrical setting. We remark that in neuroscience applications a thin layer of extracellular media is always present between different cells, i.e. $\Gamma_{ij} = \varnothing$. On the other hand, in cardiac tissue modeling, different cells are

This manuscript is for review purposes only.
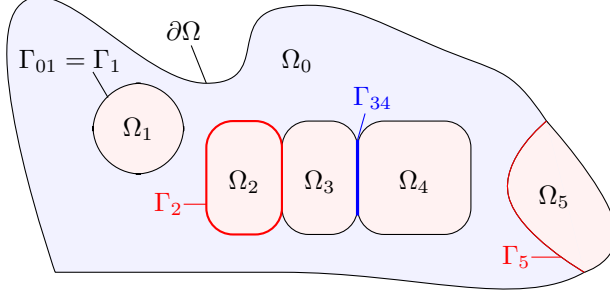
Fig. 1: Example of an EMI geometry with $N = 5$ cells with $\Omega = \left(\bigcup_{i=0}^{5} \Omega_i \right) \cup \left(\bigcup_{i=1}^{5} \Gamma_i \right)$. Here, boundary conditions are enforced only for Ω_0 and Ω_5 and Γ_{34} is an example of a common interface between two cells (e.g. a gap junction).

often in direct contact, through so-called *gap junction*, with a non-empty Γ_{ij}. We explore both applications, theoretically and experimentally.

We consider the following stationary problem for extra- and intracellular potentials■ $u_i : \overline{\Omega}_i \to \mathbb{R}$, for $i = 0, \dots, N$:

$$(2.1) \qquad -\nabla \cdot (\sigma_i \nabla u_i) = 0 \qquad\qquad \text{in } \Omega_i,$$

$$(2.2) \qquad -\sigma_i \nabla u_i \cdot \mathbf{n}_i = \sigma_j \nabla u_j \cdot \mathbf{n}_j = I_{ij} \qquad \text{in } \Gamma_{ij},\ \forall j \neq i,$$

$$(2.3) \qquad v_{ij} = u_i - u_j \qquad\qquad \text{in } \Gamma_{ij},\ \forall j \neq i,$$

$$(2.4) \qquad \tau I_{ij} = v_{ij} + f_{ij} \qquad\qquad \text{in } \Gamma_{ij},\ \forall j \neq i,$$

where $\sigma_i \in \mathbb{R}_+$ is the conductivity in Ω_i, $\mathbf{n}_i$ is the outer normal of $\partial\Omega_i$, $I_{ij} : \Gamma_{ij} \to \mathbb{R}$ is a membrane current, and $f_{ij} \in L^2(\Gamma_{ij})$ is a known membrane source satisfying $f_{ij} = -f_{ji}$, e.g. in the form

$$(2.5) \qquad\qquad f_{ij} = \begin{cases} g, & \text{for } i < j, \\ -g, & \text{for } i > j, \end{cases}$$

for a source function $g \in L^2(\Gamma)$. The physical parameter $\tau = C_M^{-1} \Delta t \in \mathbb{R}_+$ includes the membrane capacitance C_M and a discrete time step Δt. Essentially, the EMI problem consists of $N + 1$ homogeneous Poisson problems coupled at the interfaces Γ_i, where the solution can be discontinuous, via a Robin-type condition (2.2)-(2.4), In particular, eq. (2.4) is obtained by an implicit-explicit (IMEX) time discretization of the membrane current, given a capacitive and an ionic contribution:

$$I_{ij} = I_{ij,\text{cap}} + I_{ij,\text{ion}} = C_M \frac{\partial v_{ij}}{\partial t} + I_{\text{ion}}(v_{ij}).$$

The capacitive contribution $I_{ij,\text{cap}}$ satisfies the capacitor current-voltage relation and $I_{\text{ion}} : \mathbb{R} \to \mathbb{R}$ is an ionic current subject to further modelling, i.e. a possibly non-linear reaction term. Given the initial condition for the trans-membrane voltage $v_{\text{in}} : \Gamma \to \mathbb{R}$, we have $\tau^{-1}(v_{ij} - v_{\text{in}}) = I_{ij} - I_{\text{ion}}(v_{\text{in}})$ for $0 \leq i < j \leq N$ (considering $v_{ij} = -v_{ji}$ and $I_{ij} = -I_{ji}$), and define the source term in (2.5) as

$$(2.6) \qquad\qquad f = \tau I_{\text{ion}}(v_{\text{in}}) - v_{\text{in}}.$$

3
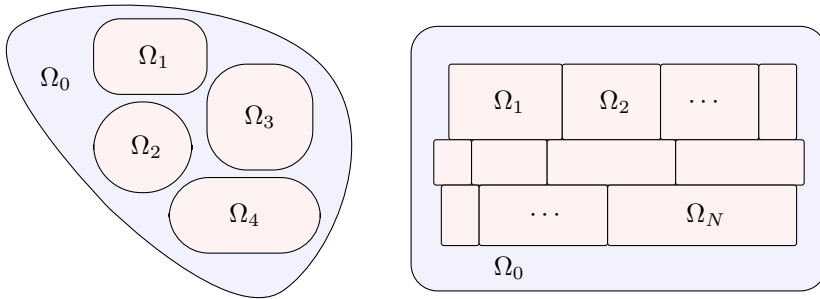
Fig. 2: Examples of geometrical setting for the nervous system (left) and cardiac tissue (right) for $d = 2$.

We close the EMI problem with homogeneous Neumann boundary conditions:

$$(2.7) \qquad \nabla u_i \cdot \mathbf{n}_i = 0 \quad \text{in} \quad \partial\Omega \cap \partial\Omega_i \quad \text{for} \quad i = 0, \dots, N.$$

Because of the pure Neumann boundary condition, the solving potentials u_i are defined up to an additive constant. Uniqueness can be enforced via Lagrange multipliers, pinning the solution in one point, or on the discrete level, providing a discrete nullspace to the solution strategy.

We investigate two cases of interest in the context of excitable tissues in physiological applications, cf. Figure 2, with final remarks on the general problem:

(i) A relevant setting to model nervous system cells. In this case, a layer of extracellular media is always present between different cells (e.g. neurons and glial cells, see for example [43]), i.e. $\Gamma_i = \Gamma_{i,0}$ for all $i = 1, \dots, N$ or, equivalently, $\Gamma_{ij} = \varnothing$ if $i, j \neq 0$.

(ii) A setting for cell-by-cell cardiac modeling. We consider the geometry of myocardiocytes, cardiac muscles cells which are connected by gap junctions or intercaleted discs, with a somehow regular pattern [31].

3. Weak formulation and discrete operators. The EMI problem can be weakly formulated in various ways, depending on the unknowns of interest. We refer to [46] for a broad discussion on various formulations (including the so-called mixed ones). As it could be expected from the structure of (2.1)-(2.4), all formulations and corresponding discretizations give rise to block operators, with different blocks corresponding to Ω_i, and Γ_{ij}.

We use a so-called *single-dimensional* formulation and the corresponding discrete operators. In this setting, the weak form depends only on bulk quantities u_i since the current term I_{ij} is replaced by:

$$I_{ij} = \tau^{-1}(u_i - u_j + f_{ij}),$$

according to equations (2.3)-(2.4).

After substituting the expression for I_{ij} in (2.2), assuming the solution u_i to be sufficiently regular over Ω_i, we multiply the PDEs in (2.1) by test functions $\phi_i \in V_i(\Omega_i)$, with V_i a sufficiently regular Sobolev space with elements satisfying the boundary conditions in (2.7); in practice $V_i = H^1(\Omega_i)$ is a standard choice. After

4

integrating over Ω_i and applying integration by parts, using the normal flux definition (2.2), we have the following variational formulation for $i = 0, \ldots, N$:

$$-\int_{\Omega_i} \nabla \cdot (\sigma_i \nabla u_i) \phi_i \, d\boldsymbol{x} = 0,$$

$$\sigma_i \int_{\Omega_i} \nabla u_i \cdot \nabla \phi_i \, d\boldsymbol{x} - \int_{\partial \Omega_i} \sigma_i \nabla u_i \cdot \mathbf{n}_i \phi_i \, ds = 0,$$

$$\sigma_i \int_{\Omega_i} \nabla u_i \cdot \nabla \phi_i \, d\boldsymbol{x} + \sum_{j \neq i} \int_{\Gamma_{ij}} I_{ij} \phi_i \, ds = 0,$$

$$\tau \sigma_i \int_{\Omega_i} \nabla u_i \cdot \nabla \phi_i \, d\boldsymbol{x} + \sum_{j \neq i} \int_{\Gamma_{ij}} (u_i - u_j + f_{ij}) \phi_i \, ds = 0.$$

Defining $\tau_i = \tau \sigma_i$, the weak EMI problem finally reads: for $i = 0, \ldots, N$, find $u_i \in V_i(\Omega_i)$ such that

$$(3.1) \qquad \tau_i \int_{\Omega_i} \nabla u_i \cdot \nabla \phi_i \, d\boldsymbol{x} + \int_{\Gamma_i} u_i \phi_i \, ds - \sum_{j \neq i} \int_{\Gamma_{ij}} u_j \phi_i \, ds = -\sum_{j \neq i} \int_{\Gamma_{ij}} f_{ij} \phi_i \, ds,$$

for all test functions $\phi_i \in V_i(\Omega_i)$. We refer to [46, Section 6.2.1] for boundedness and coercivity results for this formulation. According to (2.5), the right hand side of (3.1) can be rewritten as

$$(3.2) \qquad -\sum_{j \neq i} \int_{\Gamma_{ij}} f_{ij} \phi_i \, ds = -\sum_{i < j} \int_{\Gamma_{ij}} g \phi_i \, ds + \sum_{i > j} \int_{\Gamma_{ij}} g \phi_i \, ds.$$

For each subdomain Ω_i we construct a conforming tessellation $\mathcal{T}_i$. We then introduce a yet unspecified discretization via finite element basis functions $\{\phi_{i,j}\}_{j=1}^{n_i}$ (e.g. Lagrangian elements of order $p \in \mathbb{N}$) for $V_{i,h} \subset V_i$:

$$V_{i,h} = \text{span}\left(\{\phi_{i,k}\}_{k=1}^{n_i}\right), \quad \text{and} \quad u_i(\boldsymbol{x}) \approx u_{i,h}(\boldsymbol{x}) = \sum_{k=1}^{n_i} u_{i,k} \phi_{i,k}(\boldsymbol{x}),$$

with $n_i \in \mathbb{N}$ denoting the number of degrees of freedom in the corresponding subdomain Ω_i and $u_{i,k} \in \mathbb{R}$ the unknown coefficients. Even if the presented theory is general, in the numerical experiments, we consider the natural choice of tessellations matching at each interface Γ_i. From (3.1) we define the following discrete operators for $i = 0, \ldots, N$: bulk Laplacians

$$(3.3) \qquad A_i = \left[\int_{\Omega_i} \nabla \phi_{i,\ell}(\boldsymbol{x}) \cdot \nabla \phi_{i,k}(\boldsymbol{x}) \, d\boldsymbol{x}\right]_{\ell,k=1}^{n_i} \in \mathbb{R}^{n_i \times n_i},$$

and membrane mass matrices:

$$(3.4) \qquad M_i = \left[\int_{\Gamma_i} \phi_{i,\ell}(\boldsymbol{x}) \phi_{i,k}(\boldsymbol{x}) \, ds\right]_{\ell,k=1}^{n_i} \in \mathbb{R}^{n_i \times n_i}.$$

We then define coupling matrices for $i, j = 0, \ldots, N$ and $i \neq j$:

$$(3.5) \qquad B_{i,j} = -\left[\int_{\Gamma_{ij}} \phi_{i,\ell}(\boldsymbol{x}) \phi_{j,k}(\boldsymbol{x}) \, ds\right]_{(\ell,k)=(1,1)}^{(n_i,n_j)} \in \mathbb{R}^{n_i \times n_j},$$

5

and membrane source vectors

$$(3.6) \qquad \boldsymbol{f}_i = - \left[\sum_{j \neq i} \int_{\Gamma_{ij}} f_{ij}(\boldsymbol{x}) \phi_{i,k}(\boldsymbol{x}) \, \mathrm{d}s \right]_{k=1}^{n_i} \in \mathbb{R}^{n_i}.$$

Let us remark that the matrices M_i and B_{ij} are possibly both low rank, since have non-zero entries only corresponding to membranes Γ_i degrees of freedom, cf. eq. (3.9). We also note that $B_{i,j} = B_{j,i}^T$. We write the symmetric linear system of size $n = \sum_{i=0}^{N} n_i$ corresponding to (3.1):

(3.7)
$$\begin{bmatrix} D_0 & B_{0,1} & B_{0,2} & \cdots & & B_{0,N} \\ B_{1,0} & D_1 & B_{1,2} & & & \vdots \\ B_{2,0} & B_{2,1} & D_2 & \ddots & & B_{2,N} \\ \vdots & \ddots & \ddots & \ddots & & B_{N-1,N} \\ B_{N,0} & \cdots & B_{N,N-2} & B_{N,N-1} & & D_N \end{bmatrix} \begin{bmatrix} \boldsymbol{u}_0 \\ \boldsymbol{u}_1 \\ \boldsymbol{u}_2 \\ \vdots \\ \boldsymbol{u}_{N-1} \\ \boldsymbol{u}_N \end{bmatrix} = \begin{bmatrix} \boldsymbol{f}_0 \\ \boldsymbol{f}_1 \\ \boldsymbol{f}_2 \\ \vdots \\ \boldsymbol{f}_{N-1} \\ \boldsymbol{f}_N \end{bmatrix} \iff \mathcal{A}_{\boldsymbol{n}} \boldsymbol{u} = \boldsymbol{f},$$

with the diagonal blocks defined by

$$(3.8) \qquad D_i = \tau_i A_i + M_i, \qquad \text{for} \quad i = 0, \dots, N,$$

and $\boldsymbol{u}_i = [u_{i,0}, u_{i,1}, \dots, u_{i,n_i}] \in \mathbb{R}^{n_i}$ collecting the finite element coefficients corresponding to Ω_i. We label the coefficient matrix in (3.7) as $\mathcal{A}_{\boldsymbol{n}}$, where $\boldsymbol{n}$ is the vector $\boldsymbol{n} = (n_0, n_1, \dots, n_N)$ containing the sizes of the matrices $D_0, D_1, \dots, D_N$. By summing the entries of $\boldsymbol{n}$, we obtain the size $n = \sum_{i=0}^{N} n_i$ of $\mathcal{A}_{\boldsymbol{n}}$. Notice that if we fix the number of cells N, the domains, the type of tessellation, and the type of finite element basis functions, and only the mesh size varies, then the number n uniquely determines the vector $\boldsymbol{n}$. In this setting, we can refer to the corresponding coefficient matrix sequence, as $\{\mathcal{A}_{\boldsymbol{n}}\}_n$. Furthermore, notice that each n_i, for $i = 0, \dots, N$, is also determined by various approximation and problem parameters as the degree p, the regularity k of the global approximated solution (e.g. $k = 0$ for standard Lagrangian finite elements, $k = -1$ for discontinuous Galerkin, and $k = p-1$ in the isogeometric analysis case) and on the dimensionality d of the domain. Moreover, making the entries corresponding to Γ_i denoted explicitly (with subscript Γ), for $i = 0, \dots, N$, we can write

$$(3.9) \qquad D_i = \begin{bmatrix} D_{i,\mathrm{b}} & D_{i,\mathrm{c}} \\ D_{i,\mathrm{c}}^T & D_{i,\Gamma} \end{bmatrix}, \qquad B_{i,j} = \begin{bmatrix} 0 & 0 \\ 0 & B_{ij,\Gamma} \end{bmatrix}, \qquad M_i = \begin{bmatrix} 0 & 0 \\ 0 & M_{i,\Gamma} \end{bmatrix},$$

where $D_{i,\mathrm{b}}$ are bulk blocks, $D_{i,\mathrm{c}}$ are coupling blocks, and $D_{i,\Gamma}, B_{ij,\Gamma}$ and $M_{i,\Gamma}$ are blocks corresponding to Γ, with size $n_{i,\Gamma}$. For notational convenience, we define the total number of intracellular and membrane points,

$$n_{\mathrm{in}} = \sum_{i=1}^{N} n_i, \qquad n_\Gamma = \sum_{i=1}^{N} n_{i,\Gamma}.$$

3.1. Nervous system setting. In this setting, we have $\Gamma_{ij} = \varnothing$ for $i, j \neq 0$, i.e. the extra-diagonal blocks vanish for $i > 0$, i.e. $B_{i,j} = 0$ for $i, j > 0$ and, with abuse

6

of notation, the coefficients matrix $\mathcal{A_n}$ has the following block arrowhead form:

(3.10)
$$\mathcal{A_n} = \begin{bmatrix} D_0 & B_1 & B_2 & \cdots & B_N \\ B_1^T & D_1 & 0 & \cdots & 0 \\ B_2^T & 0 & D_2 & \ddots & \vdots \\ \vdots & \vdots & \ddots & \ddots & 0 \\ B_N^T & 0 & \cdots & 0 & D_N \end{bmatrix},$$

where $B_j \equiv B_{0,j} = B_{j,0}^T$ for notational convenience. Analytical inverses of block arrowhead matrices [42], depending only on sub-blocks inversions, can be obtained via the Sherman–Morrison–Woodbury (SMW) formula (a.k.a. Woodbury matrix identity), depending on a decomposition in the form:

(3.11)
$$\mathcal{A_n} = D_n + U_n V_n,$$

with D_n, U_n, V_n conformable matrices. According to (3.7), in the EMI case the following decomposition is a natural choice:

(3.12)
$$D_n = \begin{bmatrix} D_0 & & & \\ & D_1 & & \\ & & \ddots & \\ & & & D_N \end{bmatrix}, U_n = \begin{bmatrix} I_{n_0} & 0 \\ 0 & B_1^T \\ \vdots & \vdots \\ 0 & B_N^T \end{bmatrix}, V_n = \begin{bmatrix} 0 & B_1 & \cdots & B_N \\ I_{n_0} & 0 & \cdots & 0 \end{bmatrix}.$$

Crucially, the $D_1, \ldots, D_N$ blocks are singular, since they correspond to sub-problems with unspecified boundary conditions (i.e. a rank-one deficiency), and therefore the block diagonal matrix D_n is also singular, with $\text{rank}(D_n) = n - N$, while $U_n V_n$ has rank $2n_\Gamma$ (by numerical inspection). Thus, to apply the SMW formula, given $\epsilon > 0$, we define a full rank correction of D_n as

$$D_{n,\epsilon} = D_n + \epsilon I_n,$$

and the corresponding block arrowhead matrix

$$\mathcal{A}_{n,\epsilon} = D_{n,\epsilon} + U_n V_n,$$

with $\lim_{\epsilon \to 0} \mathcal{A}_{n,\epsilon} = \mathcal{A_n}$. Notice that the term ϵI_n could also be replaced by any term ϵE_n such that $D_n + \epsilon E_n$ is invertible for any $\epsilon > 0$. We can then apply the SMW formula to obtain $\mathcal{A}_{n,\epsilon}^{-1}$ as

(3.13)
$$\mathcal{A}_{n,\epsilon}^{-1} = D_{n,\epsilon}^{-1} - D_{n,\epsilon}^{-1} V_n (I_{2n_0} + V_n D_{n,\epsilon}^{-1} U_n)^{-1} U_n D_{n,\epsilon}^{-1},$$

which depends on $D_{n,\epsilon}^{-1}$, i.e. N independent inversions $D_0^{-1}, \ldots, D_N^{-1}$, and the solution of a linear system of size $2n_0$. Moreover, given $\lim_{\epsilon \to 0} \mathcal{A}_{n,\epsilon}^{-1} = \mathcal{A_n}^{-1}$, the form of $\mathcal{A}_{n,\epsilon}^{-1}$ can be used to design preconditioners, cf. equation (5.1). Alternatively, we introduce the following decomposition of $\mathcal{A_n}$ as

$$\mathcal{A_n} = D_n + E_n - E_n + U_n V_n,$$

with the rank N correction:

$$E_n = \begin{bmatrix} 0 & 0 & 0 & 0 \\ 0 & \mathbf{e}_{1,1}^T \mathbf{e}_{1,1} & 0 & 0 \\ 0 & 0 & \ddots & 0 \\ 0 & 0 & 0 & \mathbf{e}_{1,N}^T \mathbf{e}_{1,N} \end{bmatrix},$$

7

where $\mathbf{e}_{1,i} = [1, 0, \ldots, 0] \in \mathbb{R}^{n_i}$. We can then write

$$\mathcal{A}_{\boldsymbol{n}} = \widetilde{D}_{\boldsymbol{n}} + \widetilde{U}_{\boldsymbol{n}} \widetilde{V}_{\boldsymbol{n}},$$

with $\widetilde{D}_{\boldsymbol{n}} = D_{\boldsymbol{n}} + E_{\boldsymbol{n}}$,

$$\widetilde{U}_{\boldsymbol{n}} = \left[U_{\boldsymbol{n}} \left| \begin{array}{cccc} 0 & 0 & 0 & 0 \\ \mathbf{e}_{1,1}^T & 0 & 0 & 0 \\ 0 & \mathbf{e}_{1,2}^T & 0 & 0 \\ 0 & 0 & \ddots & 0 \\ 0 & 0 & 0 & \mathbf{e}_{1,N}^T \end{array} \right. \right], \quad \widetilde{V}_{\boldsymbol{n}} = \left[\begin{array}{c} V_{\boldsymbol{n}} \\ \hline \begin{array}{ccccc} 0 & \mathbf{e}_{1,1} & 0 & 0 & 0 \\ 0 & 0 & \mathbf{e}_{1,2} & 0 & 0 \\ 0 & 0 & 0 & \ddots & 0 \\ 0 & 0 & 0 & 0 & \mathbf{e}_{1,N} \end{array} \end{array} \right],$$

where $\widetilde{D}_{\boldsymbol{n}}$ has full rank and $\widetilde{U}_{\boldsymbol{n}} \widetilde{V}_{\boldsymbol{n}}$ is a $2n_\Gamma + N$ rank correction. Again, applying the SMW formula we obtain a closed equation for $\mathcal{A}_{\boldsymbol{n}}^{-1}$:

(3.14) $$\mathcal{A}_{\boldsymbol{n}}^{-1} = \widetilde{D}_{\boldsymbol{n}}^{-1} - \widetilde{D}_{\boldsymbol{n}}^{-1} \widetilde{V}_{\boldsymbol{n}} (I_{2n_0+N} + \widetilde{V}_{\boldsymbol{n}} \widetilde{D}_{\boldsymbol{n}}^{-1} \widetilde{U}_{\boldsymbol{n}})^{-1} \widetilde{U}_{\boldsymbol{n}} \widetilde{D}_{\boldsymbol{n}}^{-1}.$$

We emphasize that both formulae (3.13) and (3.14) are of concrete algorithmic interest when either $2n_0$ or $2n_0 + N$ are negligible compared with global matrix-size n. However, the size n_0, i.e. the number of extra-cellular degrees of freedom, still corresponds to a d-dimensional discrete Laplacian block (D_0) with $d = 2, 3$. Hence, unless one uses a symbol approach as in the Schur complement computation in [34] by means of circulant or τ based approximations, these formulae do not offer a clear efficient solution strategy.

3.2. Cardiac setting. In the cardiac setting, cells can be in direct contact, i.e. with a non-empty Γ_{ij}, and the block structure in (3.10) is lost. In particular, the structure of $\mathcal{A}_{\boldsymbol{n}}$ remains general but block sparse. More precisely, the resulting sparsity pattern has a multilevel band shape: for instance, a two-level tridiagonal with tridiagonal blocks is encountered when considering a structured cell reticulum for $d = 2$. In that specific setting, the nondiagonal blocks are essential for determining the global spectral distribution and this is the reason why a pure block diagonal preconditioner might not be effective in this case, cf. Section 5.

4. Spectral analysis. In this section, we study the spectral distribution of the matrix sequence $\{\mathcal{A}_{\boldsymbol{n}}\}_n$ in (3.10) under various assumptions for determining the global behaviour of the eigenvalues of $\mathcal{A}_{\boldsymbol{n}}$ as the matrix-size $n = \sum_{i=0}^N n_i$ tends to infinity and for a fixed number of cells N, potentially large: the limit case of $N \to \infty$ is briefly discussed in Remark 4.11. The spectral distribution is given by a smooth function called the (spectral) symbol as it is customary in the Toeplitz and Generalized Locally Toeplitz (GLT) setting [24, 25, 5, 4].

We consider in detail the setting describing cells in the nervous system, with $\mathcal{A}_{\boldsymbol{n}}$ given by (3.10). A short discussion on the cardiac setting is contained in Remark 4.12. Regarding the needed notions, we give the formal definition of Toeplitz structures, eigenvalue (spectral) and singular value distribution, few connected basic tools, and finally, we provide the specific analysis of EMI matrix sequences under a variety of assumptions.

4.1. Toeplitz structures, spectral symbol, GLT tools. We provide the definition of block Toeplitz sequences associated with a matrix-valued Lebesgue integrable function over $[-\pi, \pi]^d$, $d \geq 1$. Subsequently, we introduce the notion of eigenvalue (spectral) and singular value distribution, and we report few tools taken from the relevant literature.

DEFINITION 4.1. [Toeplitz sequences (generating function of)] *Denote by f a d-variate complex-valued integrable function, defined over the domain $Q^d = [-\pi, \pi]^d, d \geq 1$, with d-dimensional Lebesgue measure $\mu_d(Q^d) = (2\pi)^d$. Denote by f_k the Fourier coefficients of f,*

$$f_k = \frac{1}{(2\pi)^d} \int_{Q^d} f(\theta) e^{-i(k,\theta)} \, d\theta, \; k = (k_1, \cdots, k_d) \in \mathbb{Z}^d, \; i^2 = -1,$$

where $\theta = (\theta_1, \cdots, \theta_d)$, $(k, \theta) = \sum_{j=1}^d k_j \theta_j$. By following the multi-index notation in [47][Section 6], with each f we can associate a sequence of Toeplitz matrices $\{T_\nu\}_\nu$, with $\nu = (\nu_1, \cdots, \nu_d)$ being a multi-index, with the formula

$$T_\nu = \{f_{k-\ell}\}_{k,\ell=\mathbf{e}^T}^\nu \in \mathbb{C}^{N(\nu) \times N(\nu)},$$

with $\mathbf{e} = [1, 1, \cdots, 1] \in \mathbb{N}^d$ and $N(\nu) = \nu_1 \times \cdots \times \nu_d$.

For $d = 1$

$$T_\nu = \begin{bmatrix} f_0 & f_{-1} & \cdots & f_{-\nu+1} \\ f_1 & f_0 & \ddots & \vdots \\ \vdots & \ddots & f_0 & f_{-1} \\ f_{\nu-1} & \cdots & f_1 & f_0 \end{bmatrix},$$

or for $d = 2$, i.e. the two-level case, and for example $\nu = (2, 3)$, we have

$$T_\nu = \begin{bmatrix} F_0 & F_{-1} \\ F_1 & F_0 \end{bmatrix}, \quad F_k = \begin{bmatrix} f_{k,0} & f_{k,-1} & f_{k,-2} \\ f_{k,1} & f_{k,0} & f_{k,-1} \\ f_{k,2} & f_{k,1} & f_{k,0} \end{bmatrix}, \quad k = 0, \pm 1.$$

The function f is referred to as the generating function (or the symbol of) T_ν. Using a more compact notation, we say that the function f is the generating function of the whole sequence $\{T_\nu\}_\nu$ and we write $T_\nu = T_\nu(f)$.

If f is d-variate, $\mathbb{C}^{s_1 \times s_2}$ matrix-valued, and integrable over Q^d, $d, s_1, s_2 \geq 1$, i.e. $f \in L^1(Q^d, s_1 \times s_2)$, then we can define the Fourier coefficients of f in the same way (now f_k is a matrix of size $s_1 \times s_2$) and consequently $T_\nu = \{f_{k-\ell}\}_{k,\ell=\mathbf{e}^T}^\nu \in \mathbb{C}^{s_1 N(\nu) \times s_2 N(\nu)}$, then T_ν is a d-level block Toeplitz matrix according to Definition 4.1 in [9]. If $s_1 = s_2 = s$ then we write $f \in L^1(Q^d, s)$.

As in the scalar case, the function f is referred to as the generating function of T_ν. We say that the function f is the generating function of the whole sequence $\{T_\nu\}_\nu$, and we use the notation $T_\nu = T_\nu(f)$.

DEFINITION 4.2. *Let $f : D \to \mathbb{C}^{s \times s}$ be a measurable matrix-valued function with eigenvalues $\lambda_i(f)$ and singular values $\sigma_i(f)$, $i = 1, \ldots, s$. Assume that $D \subset \mathbb{R}^d$ is Lebesgue measurable with positive and finite Lebesgue measure $\mu_d(D)$. Assume that $\{A_n\}_n$ is a sequence of matrices such that $\dim(A_n) = d_n \to \infty$, as $n \to \infty$ and with eigenvalues $\lambda_j(A_n)$ and singular values $\sigma_j(A_n)$, $j = 1, \ldots, d_n$.*

- *We say that $\{A_n\}_n$ is distributed as f over D in the sense of the eigenvalues, and we write $\{A_n\}_n \sim_\lambda (f, D)$, if*

$$(4.1) \qquad \lim_{n \to \infty} \frac{1}{d_n} \sum_{j=1}^{d_n} F(\lambda_j(A_n)) = \frac{1}{\mu_d(D)} \int_D \frac{1}{s} \sum_{i=1}^s F(\lambda_i(f(t))) \, dt,$$

for every continuous function F with compact support. In this case, we say that f is the spectral symbol *of $\{A_n\}_n$.*

- *We say that $\{A_n\}_n$ is* distributed as f over D in the sense of the singular values, *and we write $\{A_n\}_n \sim_\sigma (f, D)$, if*

$$(4.2) \qquad \lim_{n \to \infty} \frac{1}{d_n} \sum_{j=1}^{d_n} F(\sigma_j(A_n)) = \frac{1}{\mu_d(D)} \int_D \frac{1}{s} \sum_{i=1}^{s} F(\sigma_i(f(t))) \, \mathrm{d}t,$$

  for every continuous function F with compact support. In this case, we say that f is the singular value symbol *of $\{A_n\}_n$.*
- *The notion $\{A_n\}_n \sim_\sigma (f, D)$ applies also in the rectangular case where f is $\mathbb{C}^{s_1 \times s_2}$ matrix-valued. In such a case the parameter s in formula (4.2) has to be replaced by the minimum between s_1 and s_2: furthermore $A_n \in \mathbb{C}^{d_n^{(1)} \times d_n^{(2)}}$ with d_n in formula (4.2) being the minimum between $d_n^{(1)}$ and $d_n^{(2)}$. Of course the notion of eigenvalue distribution does not apply in a rectangular setting.*

Throughout the paper, when the domain can be easily inferred from the context, we replace the notation $\{A_n\}_n \sim_{\lambda,\sigma} (f, D)$ with $\{A_n\}_n \sim_{\lambda,\sigma} f$.

Remark 4.3. If f is smooth enough, an informal interpretation of the limit relation (4.1) (resp. (4.2)) is that when n is sufficiently large, the eigenvalues (resp. singular values) of A_n can be subdivided into s different subsets of the same cardinality. Then d_n/s eigenvalues (resp. singular values) of A_n can be approximated by a sampling of $\lambda_1(f)$ (resp. $\sigma_1(f)$) on a uniform equispaced grid of the domain D, and so on until the last d_n/s eigenvalues (resp. singular values), which can be approximated by an equispaced sampling of $\lambda_s(f)$ (resp. $\sigma_s(f)$) in the domain D.

Remark 4.4. We say that $\{A_n\}_n$ is *zero-distributed* in the sense of the eigenvalues if $\{A_n\}_n \sim_\lambda 0$. Of course, if the eigenvalues of A_n tend all to zero for $n \to \infty$, then this is sufficient to claim that $\{A_n\}_n \sim_\lambda 0$.

For Toeplitz matrix sequences, the following theorem due to Tilli holds, which generalizes previous research along the last 100 years by Szegő, Widom, Avram, Parter, Tyrtyshnikov, and Zamarashkin (see [25, 4] and references therein).

THEOREM 4.5. [44] *Let $f \in L^1(Q^d, s_1 \times s_2)$, then $\{T_\nu(f)\}_\nu \sim_\sigma (f, Q^d)$. If $s_1 = s_2 = s$ and if f is a Hermitian matrix-valued function, then $\{T_\nu(f)\}_\nu \sim_\lambda (f, Q^d)$.*

The following theorem is useful for computing the spectral distribution of a sequence of Hermitian matrices. For the related proof, see [33, Theorem 4.3] and [34, Theorem 8]. Here, the conjugate transpose of the matrix X is denoted by X^*.

THEOREM 4.6. [33, Theorem 4.3] *Let $\{A_n\}_n$ be a sequence of matrices, with A_n Hermitian of size d_n, and let $\{P_n\}_n$ be a sequence such that $P_n \in \mathbb{C}^{d_n \times \delta_n}$, $P_n^* P_n = I_{\delta_n}$, $\delta_n \le d_n$ and $\delta_n/d_n \to 1$ as $n \to \infty$. Then $\{A_n\}_n \sim_\lambda f$ if and only if $\{P_n^* A_n P_n\}_n \sim_\lambda f$.*

With the notations of the result above, the matrix sequence $\{P_n^* A_n P_n\}_n$ is called a compression of $\{A_n\}_n$ and the single matrix $P_n^* A_n P_n$ is called a compression of A_n.

In what follows we take into account a crucial fact that is often neglected: the generating function of a Toeplitz matrix sequence and even more the spectral symbol of a given matrix sequence is not unique, except for the trivial case of either a constant generating function or a constant spectral symbol. In fact, here we report and generalize [16, Remark 1.3] and the discussion below [18, Theorem 3].

Remark 4.7. We remark that the presented tools are general and can be applied to matrix sequences stemming from a variety of discretization schemes such as isogeome-

tric analysis or finite volumes, in the spirit of the sections of books [25, 4] dedicated to applications and of the exposition paper [27].

4.2. Symbol analysis. Here, we state and prove three results which hold under reasonable assumptions. The first is provided in the maximal generality, while the second and the third can be viewed as special cases of the first. The results extend substantially those in [9][Section 4.2] where a single cell in the EMI model is considered, while the other level of generalization concerns the larger range of relations among all the various scaled time-steps and space-steps, $\tau_i = \sigma_i \tau$, h_i, $i = 0, \dots, N$.

THEOREM 4.8. *For $i = 0, \dots, N$ assume that*

$$n_{i,\Gamma} = o(\min\{n_i, n_0\}) \quad \text{for} \quad n_{i,\Gamma}, n_i \to \infty,$$
$$\lim_{n_i \to \infty} \frac{n_i}{n} = r_i \in (0, 1),$$
$$n = n_0 + n_{\text{in}} = \sum_{i=0}^{N} n_i, \quad \sum_{i=0}^{N} r_i = 1.$$

Also assume

(4.3)
$$\{D_i\}_n \sim_\lambda (f^i, D^i),$$

with $D^i \subset \mathbb{R}^{k_i}$, given f^i the ith cell symbol. Taking into consideration the matrix structures given in (3.11)-(3.12), it follows that

$$\{D_{\boldsymbol{n}}\}_n \sim_\lambda (g, [0, 1] \times D),$$
$$\{\mathcal{A}_{\boldsymbol{n}}\}_n \sim_\lambda (g, [0, 1] \times D),$$
$$\{\mathcal{A}_{\boldsymbol{n}} - D_{\boldsymbol{n}}\}_n \sim_\lambda (0, [0, 1] \times D),$$

where $D = D^0 \times D^1 \times D^2 \times \cdots \times D^N$ with

$$g(x, t_0, t_1, \dots, t_N) = \sum_{i=0}^{N} f^i(t_i) \psi_{[\hat{r}_{i-1}, \hat{r}_i]}(x),$$

$x \in [0, 1]$, $t_i \in D^i$ and $\hat{r}_{-1} = 0$, $\hat{r}_i = \hat{r}_{i-1} + r_i$, $\hat{r}_N = 1$, ψ_Z denoting the characteristic function of the set Z.

Proof As a preliminary observation, the employed Galerkin approach, independently of the specific method, and the structure of the equations imply that all the involved matrices are real and symmetric. Hence the symbols f^i, $i = 0, \dots, N$, are necessarily Hermitian matrix-valued. For the sake of notational simplicity we assume that all f^i take values into $\mathbb{C}^{s \times s}$ with a fixed s independent of the various parameters: the latter can be forced without loss of generality thanks to Remark 4.3 and Remark 4.6 in [9], where the case of different matrix-sizes in the symbols can be reduced to the same matrix-size with a trick based on the non-uniqueness of the spectral symbols. Taking into account Definition 4.2 and the assumptions, we have

(4.4)
$$\lim_{n_i \to \infty} \frac{1}{n_i} \sum_{j=1}^{n_i} F(\lambda_j(D_i)) = \frac{1}{\mu_{k_i}(D^i)} \int_{D^i} \frac{1}{s} \sum_{m=1}^{s} F(\lambda_m(f^i(t_i))) \, dt_i,$$

11

for $i = 0, \ldots, N$ and for any continuous function F with bounded support. Now we consider the $(N+1) \times (N+1)$ block diagonal matrix as in (3.12)

$$D_{\boldsymbol{n}} = \mathrm{diag}_{i=0}^{N}(D_i)$$

and a generic continuous function F with bounded support. By defining

$$\Delta(D_{\boldsymbol{n}}, F) = \frac{1}{n} \sum_{i=0}^{N} \sum_{j=1}^{n_i} F(\lambda_j(D_i)),$$

by exploiting the block diagonal structure of $D_{\boldsymbol{n}}$, we infer

$$\Delta(D_{\boldsymbol{n}}, F) = \sum_{i=0}^{N} \frac{n_i}{n} \frac{1}{n_i} \sum_{j=1}^{n_i} F(\lambda_j(D_i)).$$

As a consequence, according to (4.4) and using the spectral symbol notion, we obtain that the limit of $\Delta(D_{\boldsymbol{n}}, F)$ for $n_i \to \infty$ with $i = 0, \ldots, N$ exists and

(4.5)
$$\lim_{n_i \to \infty} \Delta(D_{\boldsymbol{n}}, F) = \sum_{i=0}^{N} \frac{r_i}{\mu_{k_i}(D^i)} \int_{D^i} \frac{1}{s} \sum_{m=1}^{s} F(\lambda_m(f^i(t_i))) \, \mathrm{d}t_i.$$

When looking at Definition 4.2, the quantity (4.5) is not in the form of the righthand side of (4.1): in fact, we observe a summation with $N+1$ different terms. The difficulty is not serious and can be overcome by enlarging the space with a fictitious domain $[0,1]$ and interpreting the sum in (4.5) as the global integral involving a step function. By leveraging the previous statement, we rewrite (4.5) as

$$\frac{1}{\mu_{k+1}(\hat{D})} \int_0^1 \mathrm{d}x \int_D \frac{1}{s} \sum_{m=1}^{s} F\left(\sum_{i=0}^{N} \lambda_m(f^i(t_i) \psi_{[\hat{r}_{i-1}, \hat{r}_i]}(x)) \right) \mathrm{d}t_0 \mathrm{d}t_1 \ldots \mathrm{d}t_N,$$

with $\hat{D} = [0,1] \times D$ and $k = \sum_{i=0}^{N} k_i$. As a consequence,

$$\{D_{\boldsymbol{n}}\}_n \sim_\lambda (g, [0,1] \times D)$$

is complete.

For the study of $\mathcal{A}_{\boldsymbol{n}}$ we notice that $\mathrm{rank}(\mathcal{A}_{\boldsymbol{n}} - D_{\boldsymbol{n}})$ depends on the matrix-sizes associated with the membrane terms. Therefore, by using the first assumption, $\mathrm{rank}(\mathcal{A}_{\boldsymbol{n}} - D_{\boldsymbol{n}}) \leq 2\sum_{i=1}^{N} n_{i,\Gamma} = o(n)$, $n = \sum_{i=0}^{N} n_i$. The latter is sufficient, by explicit computation, to claim that the related matrix-sequence is zero-distributed in the eigenvalue sense i.e. $\{\mathcal{A}_{\boldsymbol{n}} - D_{\boldsymbol{n}}\}_n \sim_\lambda 0$. Since $\mathcal{A}_{\boldsymbol{n}} = D_{\boldsymbol{n}} + R_{\boldsymbol{n}}$, $R_{\boldsymbol{n}} = \mathcal{A}_{\boldsymbol{n}} - D_{\boldsymbol{n}}$, the statement in [24, Exercise 5.3] implies directly that $\{\mathcal{A}_{\boldsymbol{n}}\}_n$ and $\{D_{\boldsymbol{n}}\}_n$ share the same distribution i.e. $\{\mathcal{A}_{\boldsymbol{n}}\}_n \sim_\lambda (g, [0,1] \times D)$ and the proof is concluded. $\bullet$

The following two corollaries simplify the statement of Theorem 4.8, under special assumptions which are satisfied for few basic discretization schemes and when dealing with elementary domains. The argument behind the possibility of writing several (indeed infinitely many) spectral symbols relies on the non-uniqueness of the spectral symbol and on the rearrangement theory: for a discussion on the matter refer to [18, 2].

COROLLARY 4.9. *With the same notations and assumptions as in Theorem 4.8, assuming that $r_i = \frac{1}{N+1}$, $i = 0, \ldots, N$ and $D^i = \tilde{D} \subset \mathbb{R}^k$, $i = 0, \ldots, N$, we deduce that*

$$\{D_{\boldsymbol{n}}\}_n \sim_\lambda \left(\mathrm{diag}(f^0, f^1, \ldots, f^N), \tilde{D} \right),$$

$$\{\mathcal{A}_{\boldsymbol{n}}\}_n \sim_\lambda \left(\mathrm{diag}(f^0, f^1, \ldots, f^N), \tilde{D} \right),$$

and $\{\mathcal{A}_{\boldsymbol{n}} - D_{\boldsymbol{n}}\}_n \sim_\lambda 0$.

Proof Under the given assumptions, the thesis of Theorem 4.8 is equivalent to the main statement, taking into account Definition 4.2 in the matrix-valued setting, i.e. relation (4.1) with diagonal matrix-valued spectral symbol and $s = N+1$. For the last statement, $\{\mathcal{A}_{\boldsymbol{n}} - D_{\boldsymbol{n}}\}_n \sim_\lambda 0$, it is sufficient to follow verbatim the same reasoning as in Theorem 4.8. ●

COROLLARY 4.10. *With the same notations and assumptions as in Theorem 4.8, assuming $f^i = f$, $D^i = \tilde{D} \subset \mathbb{R}^k$, $i = 0, \ldots, N$, we deduce that*

$$\{D_{\boldsymbol{n}}\}_n, \quad \{\mathcal{A}_{\boldsymbol{n}}\}_n \sim_\lambda (f, \tilde{D})$$

and $\{\mathcal{A}_{\boldsymbol{n}} - D_{\boldsymbol{n}}\}_n \sim_\lambda 0$.

Proof The proof of the relation $\{\tilde{A}_n\}_n, \quad \{A_n\}_n \sim_\lambda (f, \tilde{D})$ follows directly from the limit displayed in (4.5), after replacing f^i with f and necessarily D^i with D, $i = 0, \ldots, N$. The rest is again obtained verbatim as in Theorem 4.8. ●

Few remarks are in order.

Remark 4.11. According to the study in [18, 2], the spectral symbol in the Weyl sense stated Definition 4.2 is far from unique and in fact any rearrangement is still a symbol. Therefore we have infinitely many choices. For a fixed value of N, the expressions in Theorem 4.8 and Corollary 4.9 are satisfactory, but they cannot be used as N tends to infinity since either the domain $D^0 \times D^1 \times D^2 \times \cdots \times D^N$ changes dramatically with N or the size of the symbol explodes with N. However, when considering the univariate nondecreasing rearrangement ϕ_N of the symbol and under mild assumptions, the limit as N tends to infinity can be computed and this allows to understand the limit spectral symbol when the number of cells is extremely large, so allowing to treat very realistic situations.

Remark 4.12. In the cardiac setting, due to the direct contact of the cells, the block structure in (3.10) is lost and the important part of the matrix has a sparsity pattern of d-level tridiagonal type with $d \geq 2$. Hence the nondiagonal blocks are essential for determining the global spectral distribution and this is the reason why a pure block diagonal preconditioner is not robust with respect to the main parameters, since the related matrix-sequence does not capture the symbol of the discretization matrix-sequence. The analysis is not carried out in detail here and it will be the subject of further investigations.

4.3. Varying and adapting the symbol analysis. The symbol analysis given in the previous section is now critically discussed in terms of the meaning of the assumptions. First, we should consider the significance of assuming the existence of the distribution symbols f^i, $D^i \subset \mathbb{R}^{k_i}$, $i = 0, \ldots, N$, related to the various sequences $\{D_i\}_n$, associated with the blocks of $\{D_{\boldsymbol{n}}\}_n$, namely, equation (4.3). Looking at the structure of D_i, as reported in (3.8), assumption (4.3) holds if and only if

$$\lim_{h_i, \tau_i \to 0} \frac{\tau_i}{h_i^2} = c_i \in [0, \infty), \quad i = 0, \ldots, N.$$

13

Indeed, the GLT analysis of stiffness matrices arising from various discretizations (see e.g. [17, 10] for discontinuous Galerkin, [26, 16] for finite elements of any order, [15, 23, 27] for the isogeometric analysis both in Galerkin and collocation form) guarantees that there exist f^i and D^i such that

(4.6)
$$\left\{ h_i^2 A_i \right\}_n \sim_\lambda (f^i, D^i), \quad i = 0, \ldots, N,$$

and so we have

$$\{\tau_i A_i\}_n = \left\{ \frac{\tau_i}{h_i^2} h_i^2 A_i \right\}_n \sim_\lambda (c_i f^i, D^i).$$

Moreover, the rank of M_i in (3.8) is equal to the rank of $M_{i,\Gamma}$, which, in turn, is bounded by $n_{i,\Gamma} = o(\min\{n_i, n_0\})$ for $n_{i,\Gamma}, n_i \to \infty$. Therefore, the related matrix sequence is zero-distributed in the eigenvalue sense, i.e., $\{M_i\}_n \sim_\lambda 0$. Since $D_i = \tau_i A_i + M_i$, applying the statement in [24, Exercise 5.3] we get $\{D_i\}_n \sim_\lambda (c_i f^i, D^i)$.

However, we note that if $c_i = 0$ for some i, then the corresponding matrix sequences $\{D_i\}_n$ are zero-distributed in the eigenvalue sense. According to Theorem 4.8, this leads to the problem being severely ill-posed. Consequently, we choose to exclude this case from our practical consideration.

In the case where

$$\lim_{h_i, \tau_i \to 0} \frac{\tau_i}{h_i^2} = \infty, \quad i = 0, \ldots, N,$$

or where the limit above holds for some of the values $i = 0, \ldots, N$, we need to scale the matrices D_i by a factor of h_i^2/τ_i for equation (4.3) to hold. So, we perform the following scaling to the global matrix $\mathcal{A}_{\boldsymbol{n}}$

$$\mathcal{A}_{\boldsymbol{n}}^{\mathrm{s}} = \operatorname{diag}_{i=0}^N \left(\frac{h_i}{\sqrt{\tau_i}} I_{n_i} \right) \mathcal{A}_{\boldsymbol{n}} \operatorname{diag}_{i=0}^N \left(\frac{h_i}{\sqrt{\tau_i}} I_{n_i} \right)$$

and, following the same reasoning as in the proof of Theorem 4.8, we notice that

$$\mathcal{A}_{\boldsymbol{n}}^{\mathrm{s}} = \operatorname{diag}_{i=0}^N \left(\frac{h_i}{\sqrt{\tau_i}} I_{n_i} \right) D_{\boldsymbol{n}} \operatorname{diag}_{i=0}^N \left(\frac{h_i}{\sqrt{\tau_i}} I_{n_i} \right) + R_{\boldsymbol{n}}$$

with $\operatorname{rank}(R_{\boldsymbol{n}}) \leq 2 \sum_{i=1}^N n_{i,\Gamma} = o(n)$, $n = \sum_{i=0}^N n_i$. The statement in [24, Exercise 5.3] implies again that

$$\{\mathcal{A}_{\boldsymbol{n}}\}_n^{\mathrm{s}} \quad \text{and} \quad \left\{ \operatorname{diag}_{i=0}^N \left(\frac{h_i}{\sqrt{\tau_i}} I_{n_i} \right) D_{\boldsymbol{n}} \operatorname{diag}_{i=0}^N \left(\frac{h_i}{\sqrt{\tau_i}} I_{n_i} \right) \right\}_n$$

share the same distribution, namely

(4.7)
$$\{\mathcal{A}_{\boldsymbol{n}}\}_n^{\mathrm{s}} \sim_\lambda \sum_{i=0}^N f^i \psi_{[\hat{r}_{i-1}, \hat{r}_i]},$$

with $\hat{r}_{-1} = 0$, $\hat{r}_i = \hat{r}_{i-1} + r_i$, $\hat{r}_N = 1$.

In all cases, for symbols f^i, where $i = 0, \ldots, N$, each f^i maps to $\mathbb{C}^{s_i \times s_i}$, where the dimension s_i is determined by GLT theory as $s_i = (p_i - k_i)^d$. Here, d is the physical dimension of the domain (generally $d = 2$ or $d = 3$), while p_i is the degree of the polynomial in the Galerkin approach, k_i the global regularity of the approximated solution. More precisely we have $k_i = 0$ in standard Lagrangian finite elements, $k_i = -1$ in the discontinuous Galerkin method, $k_i = p_i - 1$ when using isogeometric analysis, and $0 < k_i < p_i - 1$, $p_i \geq 2$, in the case of intermediate regularity: see [27] for detailed exposition and review paper when $d = 1$ and the sections of applications in [4] for problems in multidimensional domains when $d > 1$.

14

Cells N	1	25	441	7225	116281
Extracell. dofs n_0	789504	647400	626824	696600	934344
Intracell. dofs n_{in}	263169	416025	480249	924800	1046529
Membrane dofs n_Γ	2048	12800	56448	231200	930248
Total dofs $n = n_0 + n_{\text{in}}$	1052673	1063425	1107073	1621400	1980873
n_Γ/n	0.002	0.012	0.051	0.143	0.470

Table 1: Model A: example of number of degrees of freedom corresponding to various regions for $N_h = 1024$, i.e. $(N_h + 1)^2 = 1050625$ grid points, varying the number of cells N.

5. Solution strategy and numerical experiments.

5.1. Problem and discretization settings. For $i = 0, \dots, N$ we set $\sigma_i = 1$ in (2.1)-(2.2) so that $\tau_i = \tau$ for all i. If not mentioned otherwise, we set $\tau = 0.01$ in (2.4)-(2.6). We set a passive ionic current in (2.6), i.e. $I_{\text{ion}}(v) = v$, and an oscillating initial membrane stimulus

$$v_{\text{in}} = \frac{1}{2}\sin\left(10\|\boldsymbol{x}\|^2\right) \quad \text{for} \quad \boldsymbol{x} \in \Gamma,$$

resulting in the right hand side $g = v_{\text{in}}(1 - \tau)$, with reference to (2.5),(2.6) and (3.2), cf. Figure 4. We remark that different choices of right hand sides would not alter the essence of this work. In terms of geometry, we consider three different settings: idealized (model A and B) or realistic (model C), described in the following sections.

5.2. Model A: idealized nervous system setting. In the context of Section 3.1, we consider the domain $\Omega = (0, 1)^2$. We define the N-cells partitioning function

$$\psi(x, y) = (x(3N + 1) \mod 3, \; y(3N + 1) \mod 3),$$

and the extra- and intracellular regions are respectively given by:

$$\Omega_0 = \{(x, y) \in \Omega \mid \min(\psi(x, y)) \leq 1\},$$
$$\Omega_1 \cup \Omega_2 \cup \dots \cup \Omega_N = \{(x, y) \in \Omega \mid \min(\psi(x, y)) \geq 1\}$$

cf. Figure 3. The domain Ω is discretized with with a triangular tessellation with N_h elements per side, with a total number of degrees of freedom $n = n_0 + n_{\text{in}} = \sum_{i=0}^{N} n_i$ given $(N_h + 1)^2$ grid points. Assuming that N_h is a power of 2, the number of cells is chosen of the form $N = \left(\frac{2^{2k} - 1}{3}\right)^2$, with $k = 1, 2, \dots, \lceil(\log_2 N_h)/2\rceil$, so that the geometry is compatible with the tessellation and the interfaces Γ_i are well defined on the mesh. In this setting, the same number of degrees of freedom $n_i = n_{\text{in}}/N$ corresponds to all cells $i = 1, \dots, N$, and n_0, n_{in}, and n_Γ depend on N cf. Table 1 and Figure 3. The overall solution, denoted by u, including $u_0, \dots, u_N$ and the membrane initial condition v_{in} are shown in Figure 4 for $N = 1$ and $N = 25$.

5.3. Model B: idealized myocytes. In the context of Section 3.2, we consider the domain $\Omega = (0, 1)^2$ and the intracellular subdomains $\Omega_1 \cup \Omega_2 \cup \dots \cup \Omega_N = (1/8, 7/8)^2$. Again, Ω is discretized using a triangular tessellation with N_h elements per side, with N_h a power of two. The N cells are disposed in a regular $\sqrt{N} \times \sqrt{N}$ grid. Each cell corresponds to $(1 + \frac{3N_h}{4\sqrt{N}})^2$ degrees of freedom, so that the total number of intracellular degrees of freedom is $n_{\text{in}} = N \cdot (1 + \frac{3N_h}{4\sqrt{N}})^2$ and extracellular ones $n_0 = \frac{7}{2}N_h(N_h/8 + 1)$. Examples of this geometry and corresponding solutions are reported in Figure 5.

15

$$N = 25 \qquad\qquad N = 441 \qquad\qquad N = 7225$$
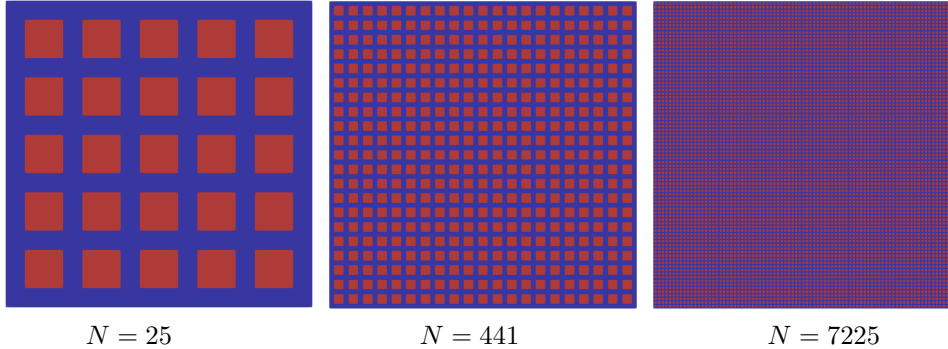
Fig. 3: Model A: two dimensional geometry varying the number of cells N. The extracellular space Ω_0 is colored in blue, while cells $\Omega_1, \Omega_2, \ldots, \Omega_N$ in red. No gap junction are present, i.e. $\Gamma_{ij} = varnothing$ for $i, j \neq 0$.

Cells N	10	50	100	200
Extracell. dofs n_0	185918	371684	467421	635518
Intracell. dofs n_{in}	139677	364293	487399	319302
Membrane dofs n_Γ	104547	298463	423930	609369
Total dofs $n = n_0 + n_{\text{in}}$	325595	735977	954820	1327301
n_Γ/n	0.32	0.41	0.44	0.46

Table 2: Model C: number of degrees of freedom corresponding to various regions varying the number of cells N.

5.4. Model C: mouse visual cortex tissue. We consider tetrahedral meshes of a dense reconstruction of the mouse visual cortex at extreme resolution. The dataset is based on the Cortical MM^3 dataset[1] centred at position (225182,107314,22000) with a resolution of $32 \times 32 \times 40 \, \text{nm}^3$. The meshed domains are cubes with side length 10 μm and include the largest 10, 50, 100 and 200 cells in the respective tissue volume, respectively, cf. Figure 6 and Table 2 for geometrical data. The domain is scaled so that $\Omega = (0, 1)^3$. We show a model C solution and membrane potential in Figure 7. We remark that the geometrical setting is different w.r.t. Table 1 for model A, since the tessellation in model C is changing to accommodate for new cells and the insertion of new cells does not modify the existing ones.

5.5. Implementation and solution strategies. We use FEniCS [1, 32] for parallel finite element assembly and `multiphenics`[2] to handle multiple meshes with common interfaces and the corresponding mixed-dimensional weak forms[3]. FEniCS wraps PETSc parallel solution strategies. For multilevel preconditioning, we use a single iteration of `hypre boomerAMG` algebraic multigrid[4] (AMG_1) [22]. For comparative studies, we use incomplete LU (ILU) preconditioning with zero fill-in. Parallel ILU is obtained via a block Jacobi preconditioner, where each block inverse is approximated
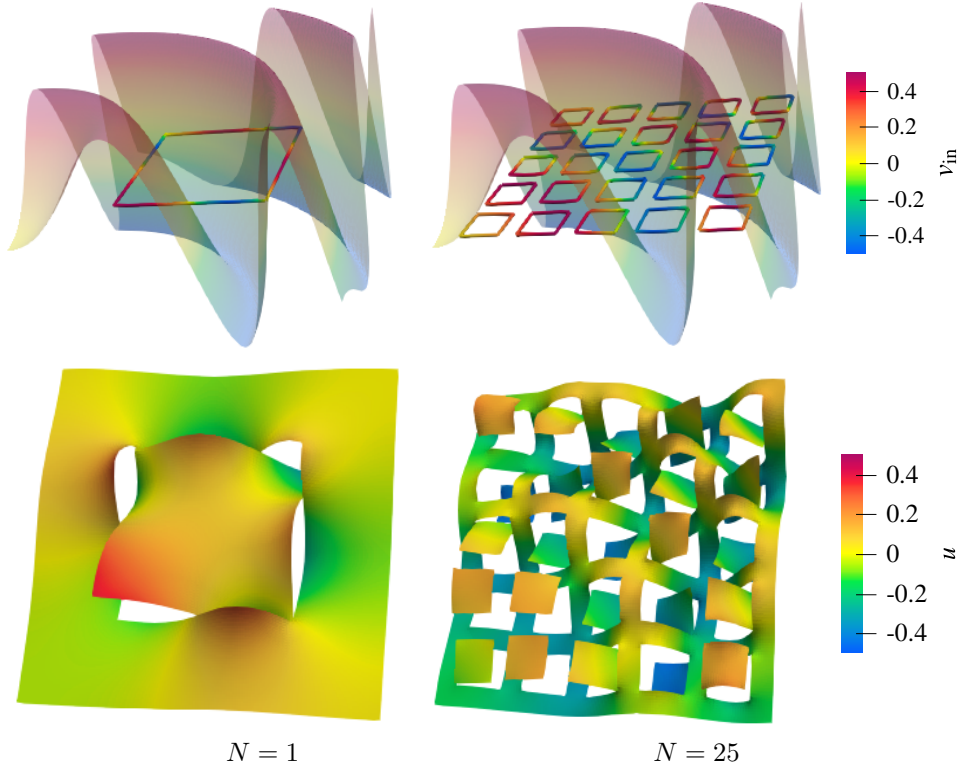
---

[1] https://www.microns-explorer.org/cortical-mm3
[2] https://multiphenics.github.io/index.html
[3] For the corresponding open software visit https://github.com/pietrobe/EMIx
[4] We use default options, only for $d = 3$ we set the strong coupling threshold to 0.5.

Fig. 4: Model A. First row: overall initial conditions $v_{\text{in}}(x, y)$ for $N = 1$ (left) and $N = 25$ (right). While v_{in} is imposed only for $(x, y) \in \Gamma$, we also show it in the whole domain Ω. Second row: corresponding solutions for $N_h = 128$.

by ILU. For iterative strategies, as stopping criteria, we use a tolerance of 10^{-9} for the relative residual. Given the pure Neumann boundary conditions (2.7), uniqueness is enforced by setting a point-wise boundary condition $u_0(\mathbf{0}) = 0$. Run-times are reported for a 2021 MacBook Pro with an M1 Pro chip, 8 cores, and 16 GB of memory. When not mentioned otherwise, experiments are performed in serial.

Following (3.14), the analysis in [9], and Theorem 4.8, we also introduce the block diagonal preconditioner, for $\epsilon > 0$,

$$
(5.1) \quad P_{\epsilon, \mathbf{n}} = \tau \begin{bmatrix} A_0 + \epsilon \widetilde{M}_0 & & & & \\ & A_1 + \epsilon \widetilde{M}_1 & & & \\ & & A_2 + \epsilon \widetilde{M}_2 & & \\ & & & \ddots & \\ & & & & A_N + \epsilon \widetilde{M}_N \end{bmatrix} \in \mathbb{R}^{n \times n},
$$

where the bulk Laplacians A_i, for $i = 0, \ldots, N$, are regularized adding the corresponding bulk mass matrices

$$
\widetilde{M}_i = \left[\int_{\Omega_i} \phi_{i,\ell}(\boldsymbol{x}) \phi_{i,k}(\boldsymbol{x}) \, d\boldsymbol{x} \right]_{\ell,k=1}^{n_i} \in \mathbb{R}^{n_i \times n_i}.
$$

17
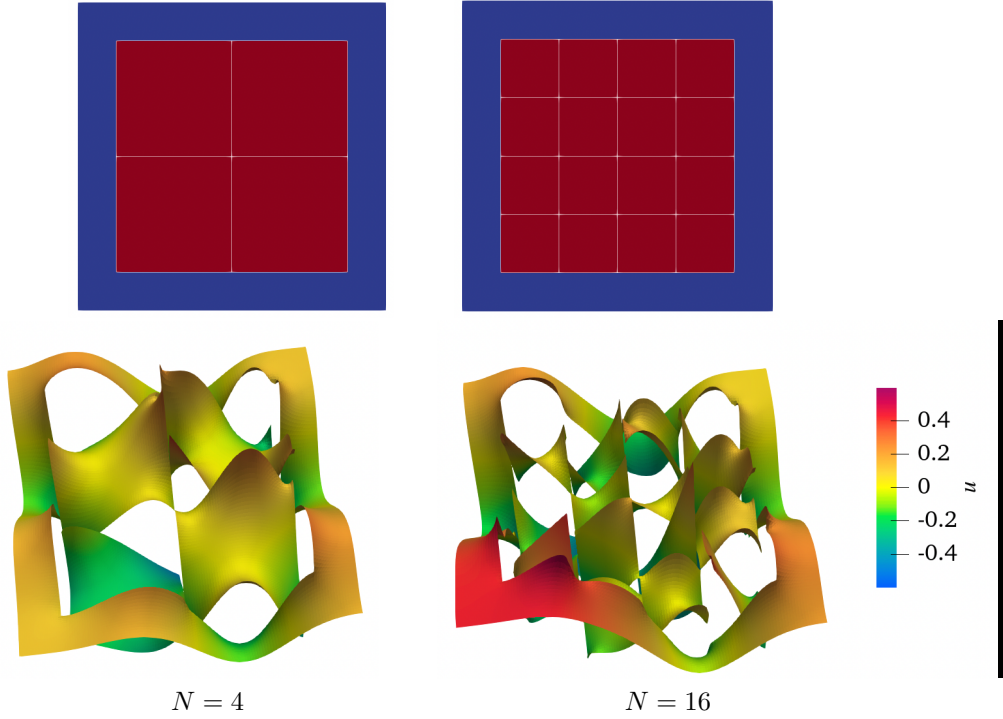
Fig. 5: Model B. First row: 2D geometry with $N = 4$ and $N = 16$ cells; the extra-cellular space Ω_0 is colored in blue, while cells $\Omega_1, \ldots, \Omega_N$ in red and membranes in white. Second row: corresponding solutions $u_0, \ldots, u_N$ for $N_h = 512$.

Let us remark that, while M_i corresponds to degrees of freedom in Γ_i, the matrix $\widetilde{M_i}$ refers to Ω_i, and is necessary as a full-rank correction to A_i, which is rank-1 deficient, lacking boundary conditions.

From a theoretical point of view, a few facts have to be emphasized as a consequence of the theoretical analysis. First, we notice that

$$(5.2) \qquad \{\mathcal{A_n} - P_{\epsilon,n}\}_n \sim_\lambda 0$$

for any $\epsilon > 0$ thanks to the different scaling of the mass and stiffness matrices, in accordance with the analysis in Section 4.2 and especially in Section 4.3. Therefore the two matrix-sequences $\{\mathcal{A_n}\}_n$, $\{P_{\epsilon,n}\}_n$ share the same distribution and more importantly

$$(5.3) \qquad \{P_{\epsilon,n}^{-1}\mathcal{A_n} - I_n\}_n \sim_\lambda 0$$

because both $\{\mathcal{A_n}\}_n$, $\{P_{\epsilon,n}\}_n$ are sparsely vanishing (see [24, Definition 8.2]), i.e. its common distribution has a determinant vanishing in a set of zero Lebesgue measure in agreement with [4, Proposition 2.27]. We remark that (5.3) is an important indication that the considered preconditioning strategy is effective. For more analysis, also in connection with outliers, we refer to [9, Section 4.4], where the case of a single cell ($N = 1$) was treated in detail.

5.6. Results. We test the convergence of various preconditioners for the CG solver, to highlight which is the more appropriate, depending on the application

18
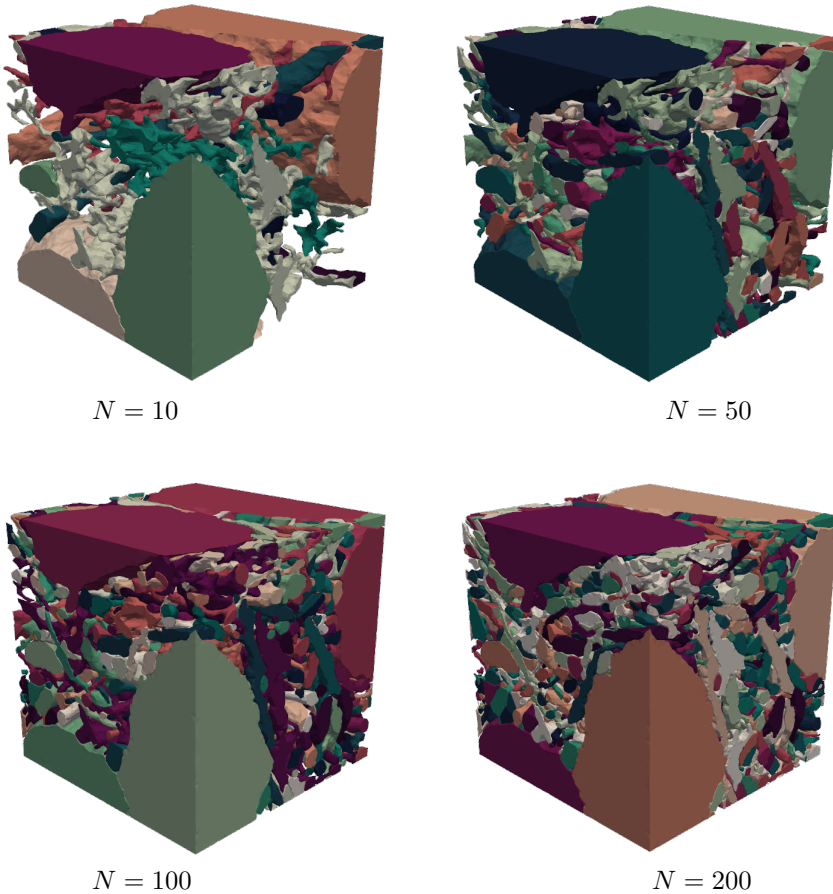
Fig. 6: Model C. For $N = 10$ the largest ten cells in the dataset are included; four neuronal somas and few glial cells are visible. As N increases the extracellular space is filled with more and more glial cells.

of interest. The block diagonal preconditioner $P_{\epsilon,\boldsymbol{n}}$ is solved to full precision with Cholesky from MUMPS and labelled as P_ϵ-CG, using $\epsilon = 10^{-4}$ for models A,B, and $\epsilon = 1$ for model C. As a preliminary experiment, in Table 3, we consider both model A and B, with a fixed number of cells N and refining the mesh. Compared to CG or ILU-CG, both the block preconditioned CG and the multilevel preconditioner are essentially robust w.r.t. N_h. Interestingly, P_ϵ-CG is less effective and robust in the cardiac setting (Model B), for which the latter theory cannot be directly applied. The direct computation of $P_\epsilon^{-1}\mathcal{A}_n$ spectrum shows a constant number of outliers (e.g. outside the interval $[1-\epsilon, 1+\epsilon]$), which are not captured by the spectral analysis, and can explain the observed convergence. The analysis of the outliers is quite involved especially in the preconditioned case and need specific tools; see [37, 39, 40] and references therein. In Table 4, we asses robustness w.r.t. the temporal discretization parameter τ for the preconditioning strategies. As expected from equation (3.8) and the discussion in Section 4.3, the block diagonal preconditioner is not robust as $\tau \to 0$. Surprisingly, AMG$_1$-CG is effective also in this scenario.

19
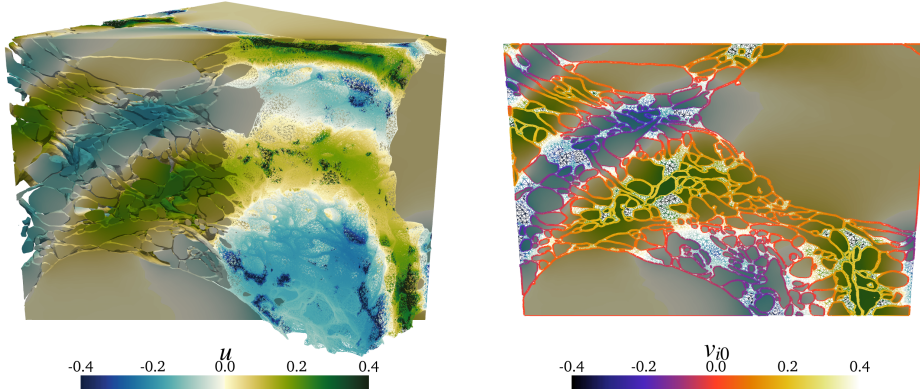
Fig. 7: Model C with $N = 200$ cells: potentials $u_0, \ldots, u_N$ on the clipped 3D domain (left) and a 2D domain slice (right), additionally highlighting the membrane potential v_{i0} with $i = 1, \ldots, N$. For the extracellular space Ω_0, the corresponding mesh is shown. The colorbar for the potential applies to the intra- and extracellular potential in both plots.

	N_h	64	128	256	512	1024
Model A	CG	392	743	1437	2725	5471
$N = 441$	ILU-CG	103	178	320	600	1694
	P_ϵ-CG	46	53	58	61	61
	AMG_1-CG	8	8	9	10	10
Model B	CG	535	954	1810	3506	6931
$N = 576$	ILU-CG	129	188	327	627	1235
	P_ϵ-CG	1040	1129	1221	1256	1352
	AMG_1-CG	9	9	10	10	12

Table 3: Iterations to convergence for various iterative methods with a fixed number of cells $N = 441$ (resp. $N = 576$) for model A (resp. B) and refining spatial discretization via N_h.

In the following results, we consider an increasing number of cells N for a fixed discretization. These experiments are of interest for at least two reasons:

(i) relevant portions of realistic tissue are typically densely populated by many different cells. In particular, in the neuroscience context, membranes have complex morphologies and the membrane degrees of freedom n_Γ are not negligible w.r.t. n, unless aggressive mesh refinement is used, cf. Figure 6 and Table 2;

(ii) as N increases, also n_Γ increases, challenging the hypothesis of Theorem 4.8. According to Tables 5-6, the block diagonal preconditioner P_ϵ is effective only for model A, and the monolithic multilevel strategy AMG_1-CG is effective and robust in both cases. This superior performance of AMG_1-CG can be attributed to the spectral properties of the whole coefficient matrix-sequence, which exhibits Laplacian-like characteristics in the related eigenvalue distribution, regardless of the specific setting. As expected from theory, P_ϵ-CG is less effective as N increases, since the first hypothesis in Theorem 4.8 is no longer satisfied. Furthermore, as already observed at the

20

τ	0.1	0.01	0.001	0.0001	0.00001
ILU-CG	1208	943	786	763	787
P_ϵ-CG	27	61	139	211	226
AMG$_1$-CG	11	9	8	8	7

Table 4: Model A: iterations to convergence for various iterative methods with fixed spatial discretization $N_h = 512$, the number of cells $N = 441$, and varying time step τ. Results using 8 cores.

beginning of Section 3.2 and in Remark 4.12, the block diagonal preconditioner cannot be satisfactory for model B, since it does not capture the spectral distribution of the original coefficient matrices.

Similarly, for the realistic model C, we report run-times and iteration counts in Table 6 for an increasing number of cells N, showing robustness and efficiency for both the ILU and the AMG$_1$ preconditioners (competitive, e.g., w.r.t. the timing results in [30]). In this case the block preconditioner P_ϵ is never viable. Let us remark that multilevel monolithic solution strategies showcase good scalability when employed on large-scale problems using massively parallel machines [7, 8].

N	1	25	441	7225	116281
ILU-CG	1796	1713	1920	1909	2353
P_ϵ-CG	57	129	276	610	1112
AMG$_1$-CG	9	9	11	11	8

Table 5: Model A: iterations to convergence of various iterative schemes fixing the spatial discretization with $N_h = 1024$, i.e. $(N_h + 1)^2 = 1050625$ grid points. Results using 8 cores.

N	1	16	256	576	4096
ILU-CG	577	588	614	627	704
P_ϵ-CG	65	305	969	1256	2295
AMG$_1$-CG	8	9	10	10	11

Table 6: Model B: iterations to convergence of various iterative schemes fixing the spatial discretization with $N_h = 512$, i.e. $(N_h + 1)^2 = 263169$ grid points.

6. Concluding remarks. We described a numerical scheme for approximating the solution of the EMI equations under the assumptions of N distinct cells. We showed the structure and spectral features of the coefficient matrices obtained from Galerkin discretizations, which are spectrally described by an appropriate linear combi‐nation of Laplacian symbols, cf. Theorem 4.8. This information suggests the use of both block diagonal preconditioners and multilevel strategies to accelerate Krylov solvers, when the spectral analysis hypotheses are satisfied. Realistic settings might challenge these hypotheses and we can expect degradation of block preconditioner performance, as we observe in the numerical experiments. In practice, a single monolithic multigrid iteration is the most robust strategy, according to the presented tests. Geometrical dependencies on convergence have yet to be fully understood. In

21

N	10	50	100	200
ILU-CG	0.9 [248]	3.0 [320]	3.9 [257]	6.3 [368]
P_ϵ-CG	66 [1069]	397 [2220]	812 [2344]	1224 [2452]
AMG$_1$-CG	1.4 [11]	4.2 [12]	6.3 [13]	9.2 [12]

Table 7: Model C: run-times (s) and iterations (in square brackets) to convergence of ILU and AMG$_1$ preconditioners, compered to a direct approach, increasing the number of cells N with geometries according to Table 2. Results using 8 cores.

general, many open problems remain, e.g., the precise study of the outliers, of their number, and of the asymptotic behavior with respect to the matrix-size and fineness parameters: using, e.g., the tools given in [37, 39, 40]. Finally, with regard to the SMW formulae (3.13) and (3.14), beside their algebraic structure, it is of interest to perform a GLT based spectral analysis. The difficulty is represented by the presence of rectangular terms (as $U_{\boldsymbol{n}}, V_{\boldsymbol{n}}, \widetilde{U}_{\boldsymbol{n}}, \widetilde{V}_{\boldsymbol{n}}$), but this can be overcome by using quite recent extensions of the GLT theory as that in [3]. However, the GLT analysis and the design of symbol-based preconditioners as in [34] are not immediate and they are beyond the scope of the current work.

Data availability. The used open software is available at https://doi.org/10.5281/zenodo.10728462 [11]. Data sets generated during the current study are available from the corresponding author on reasonable request.

Conflict of interest. The authors declare that they have no conflict of interest.

REFERENCES

[1] M. Alnæs, J. Blechta, J. Hake, A. Johansson, B. Kehlet, A. Logg, C. Richardson, J. Ring, M. E. Rognes, and G. N. Wells, *The FEniCS project version 1.5*, Archive of Numerical Software, 3 (2015), pp. 9–23.

[2] G. Barbarino, D. Bianchi, and C. Garoni, *Constructive approach to the monotone rearrangement of functions*, Expositiones Mathematicae, 40 (2022), pp. 155–175.

[3] G. Barbarino, C. Garoni, M. Mazza, and S. Serra-Capizzano, *Rectangular GLT sequences*, Electron. Trans. Numer. Anal., 55 (2022), pp. 585–617.

[4] G. Barbarino, C. Garoni, and S. Serra-Capizzano, *Block generalized locally Toeplitz sequences: theory and applications in the multidimensional case*, Electronic Transactions on Numerical Analysis, 53 (2020), pp. 113–216.

[5] G. Barbarino, C. Garoni, and S. Serra-Capizzano, *Block generalized locally Toeplitz sequences: theory and applications in the unidimensional case*, Electronic Transactions on Numerical Analysis, 53 (2020), pp. 28–112.

[6] T. M. Bartol, D. X. Keller, J. P. Kinney, C. L. Bajaj, K. M. Harris, T. J. Sejnowski, and M. B. Kennedy, *Computational reconstitution of spine calcium transients from individual proteins*, Frontiers in synaptic neuroscience, 7 (2015), p. 17.

[7] P. Benedusi, A. J. Ellingsrud, H. Herlyng, and M. E. Rognes, *Scalable approximation and solvers for ionic electrodiffusion in cellular geometries*, arXiv preprint arXiv:2403.04491, (2024).

[8] P. Benedusi, P. Ferrari, C. Garoni, R. Krause, and S. Serra-Capizzano, *Fast parallel solver for the space-time IgA-DG discretization of the diffusion equation*, Journal of Scientific Computing, 89 (2021), p. 20.

[9] P. Benedusi, P. Ferrari, M. Rognes, and S. Serra-Capizzano, *Modeling excitable cells with the EMI equations: spectral analysis and iterative solution strategy*, Journal of Scientific Computing, 98 (2024), p. 58.

[10] P. Benedusi, C. Garoni, R. Krause, X. Li, and S. Serra-Capizzano, *Space-time FE-DG discretization of the anisotropic diffusion equation in any dimension: the spectral symbol*, SIAM Journal on Matrix Analysis and Applications, 39 (2018), pp. 1383–1420.

[11] P. Benedusi and M. E. Rognes, *Scalable approximation and solvers for ionic electrodiffusion in cellular geometries*, 2024, doi:https://doi.org/10.5281/zenodo.10728462.

[12] A. P. Buccino, M. Kuchta, J. Schreiner, and K.-A. Mardal, *Improving neural simulations with the EMI model*, Springer, 2021, pp. 87–98.

[13] C. Calì, M. Agus, K. Kare, D. J. Boges, H. Lehväslaiho, M. Hadwiger, and P. J. Magistretti, *3D cellular reconstruction of cortical glia and parenchymal morphometric analysis from serial block-face electron microscopy of juvenile rat*, Progress in neurobiology, 183 (2019), p. 101696.

[14] G. R. de Souza, R. Krause, and S. Pezzuto, *Boundary integral formulation of the cell-by-cell model of cardiac electrophysiology*, arXiv preprint arXiv:2302.05281, (2023).

[15] M. Donatelli, C. Garoni, C. Manni, S. Serra-Capizzano, and H. Speleers, *Spectral analysis and spectral symbol of matrices in isogeometric collocation methods*, Mathematics of Computation, 85 (2016), pp. 1639–1680.

[16] A. Dorostkar, M. Neytcheva, and S. Serra-Capizzano, *Spectral analysis of coupled PDEs and of their Schur complements via generalized locally Toeplitz sequences in 2D*, Computer Methods in Applied Mechanics and Engineering, 309 (2016), pp. 74–105.

[17] M. Dumbser, F. Fambri, I. Furci, M. Mazza, S. Serra-Capizzano, and M. Tavelli, *Staggered discontinuous Galerkin methods for the incompressible Navier–Stokes equations: spectral analysis and computational results*, Numerical Linear Algebra with Applications, 25 (2018), p. e2151.

[18] S.-E. Ekström and S. Serra-Capizzano, *Eigenvalues and eigenvectors of banded Toeplitz matrices and the related symbols*, Numerical Linear Algebra with Applications, 25 (2018), p. e2137.

[19] A. J. Ellingsrud, P. Benedusi, and M. Kuchta, *A splitting, discontinuous Galerkin solver for the cell-by-cell electroneutral Nernst-Planck framework*, 2024, arXiv:2404.08320.

[20] A. J. Ellingsrud, C. Daversin-Catty, and M. E. Rognes, *A cell-based model for ionic electrodiffusion in excitable tissue*, Springer International Publishing, 2021.

[21] A. J. Ellingsrud, A. Solbrå, G. T. Einevoll, G. Halnes, and M. E. Rognes, *Finite element simulation of ionic electrodiffusion in cellular geometries*, Frontiers in Neuroinformatics, 14 (2020), p. 11.

[22] R. D. Falgout and U. M. Yang, *hypre: A library of high performance preconditioners*, in Computational Science—ICCS 2002: International Conference Amsterdam, The Netherlands, April 21–24, 2002 Proceedings, Part III, Springer, 2002, pp. 632–641.

[23] C. Garoni, C. Manni, S. Serra-Capizzano, D. Sesana, and H. Speleers, *Spectral analysis and spectral symbol of matrices in isogeometric Galerkin methods*, Mathematics of Computation, 86 (2017), pp. 1343–1373.

[24] C. Garoni and S. Serra-Capizzano, *Generalized locally Toeplitz sequences: theory and applications*, vol. 1, Springer, 2017.

[25] C. Garoni and S. Serra-Capizzano, *Generalized locally Toeplitz sequences: theory and*

applications, vol. 2, Springer, 2018.

[26] C. GARONI, S. SERRA-CAPIZZANO, AND D. SESANA, *Spectral analysis and spectral symbol of d-variate $\mathbb{Q}_{\mathbf{p}}$ lagrangian FEM stiffness matrices*, SIAM Journal on Matrix Analysis and Applications, 36 (2015), pp. 1100–1128.

[27] C. GARONI, H. SPELEERS, S.-E. EKSTRÖM, A. REALI, S. SERRA-CAPIZZANO, AND T. J. R. HUGHES, *Symbol-based analysis of finite element and isogeometric B-spline discretizations of eigenvalue problems: exposition and review*, Archives of Computational Methods in Engineering, 26 (2019), pp. 1639–1690.

[28] N. M. M. HUYNH, F. CHEGINI, L. F. PAVARINO, M. WEISER, AND S. SCACCHI, *Convergence analysis of BDDCpreconditioners for hybrid DG discretizations of the cardiac cell-by-cell model*, arXiv preprint arXiv:2212.12295, (2022).

[29] K. H. JÆGER, A. G. EDWARDS, W. R. GILES, AND A. TVEITO, *From millimeters to micrometers; re-introducing myocytes in models of cardiac electrophysiology*, Frontiers in Physiology, 12 (2021), p. 763584.

[30] K. H. JÆGER, K. G. HUSTAD, X. CAI, AND A. TVEITO, *Efficient numerical solution of the EMI model representing the extracellular space (E), cell membrane (M) and intracellular space (I) of a collection of cardiac cells*, Frontiers in Physics, 8 (2021), p. 579461.

[31] A. G. KLÉBER AND Y. RUDY, *Basic mechanisms of cardiac impulse propagation and associated arrhythmias*, Physiological reviews, 84 (2004), pp. 431–488.

[32] A. LOGG, K.-A. MARDAL, AND G. WELLS, *Automated solution of differential equations by the finite element method: The FEniCS book*, vol. 84, Springer Science & Business Media, 2012.

[33] M. MAZZA, A. RATNANI, AND S. SERRA-CAPIZZANO, *Spectral analysis and spectral symbol for the 2D curl-curl (stabilized) operator with applications to the related iterative solutions*, Mathematics of Computation, 88 (2019), pp. 1155–1188.

[34] M. MAZZA, M. SEMPLICE, S. SERRA-CAPIZZANO, AND E. TRAVAGLIA, *A matrix-theoretic spectral analysis of incompressible Navier–Stokes staggered DG approximations and a related spectrally based preconditioning approach*, Numerische Mathematik, 149 (2021), pp. 933–971.

[35] Y. MORI AND C. PESKIN, *A numerical method for cellular electrophysiology based on the electrodiffusion equations with internal boundary conditions at membranes*, Communications in Applied Mathematics and Computational Science, 4 (2009), pp. 85–134.

[36] A. MOTTA, M. BERNING, K. M. BOERGENS, B. STAFFLER, M. BEINING, S. LOOMBA, P. HENNIG, H. WISSLER, AND M. HELMSTAEDTER, *Dense connectomic reconstruction in layer 4 of the somatosensory cortex*, Science, 366 (2019).

[37] D. NOUTSOS, S. SERRA-CAPIZZANO, AND P. VASSALOS, *Matrix algebra preconditioners for multilevel toeplitz systems do not insure optimal convergence rate*, Theoretical Computer Science, 315 (2004), pp. 557–579.

[38] G. ROSILHO DE SOUZA, R. KRAUSE, AND S. PEZZUTO, *Boundary integral formulation of the cell-by-cell model of cardiac electrophysiology*, Engineering Analysis with Boundary Elements, 158 (2024), pp. 239–251.

[39] S. SERRA-CAPIZZANO, *Matrix algebra preconditioners for multilevel toeplitz matrices are not superlinear*, Linear algebra and its applications, 343 (2002), pp. 303–319.

[40] S. SERRA-CAPIZZANO AND P. TILLI, *Extreme singular values and eigenvalues of non-hermitian block toeplitz matrices*, Journal of computational and applied mathematics, 108 (1999), pp. 113–130.

[41] A. SHAPSON-COE, M. JANUSZEWSKI, D. R. BERGER, A. POPE, Y. WU, T. BLAKELY, R. L. SCHALEK, P. H. LI, S. WANG, J. MAITIN-SHEPARD, ET AL., *A petavoxel fragment of human cerebral cortex reconstructed at nanoscale resolution*, Science, 384 (2024), p. eadk4858.

[42] P. S. STANIMIROVIĆ, V. N. KATSIKIS, AND D. KOLUNDŽIJA, *Inversion and pseudoinversion of block arrowhead matrices*, Applied Mathematics and Computation, 341 (2019), pp. 379–401.

[43] D. STERRATT, B. GRAHAM, A. GILLIES, G. EINEVOLL, AND D. WILLSHAW, *Principles of computational modelling in neuroscience*, Cambridge University Press, 2023.

[44] P. TILLI, *A note on the spectral distribution of Toeplitz matrices*, Linear and Multilinear Algebra, 45 (1998), pp. 147–159.

[45] A. TVEITO, K. H. JÆGER, M. KUCHTA, K.-A. MARDAL, AND M. E. ROGNES, *A cell-based framework for numerical modeling of electrical conduction in cardiac tissue*, Frontiers in Physics, (2017), p. 48.

[46] A. TVEITO, K.-A. MARDAL, AND M. E. ROGNES, *Modeling excitable tissue: the EMI framework*, Springer, 2021.

[47] E. E. Tyrtyshnikov, *A unifying approach to some old and new theorems on distribution and clustering*, Linear algebra and its applications, 232 (1996), pp. 1–43.

[48] P. Velicky, E. Miguel, J. M. Michalska, J. Lyudchik, D. Wei, Z. Lin, J. F. Watson, J. Troidl, J. Beyer, Y. Ben-Simon, et al., *Dense 4d nanoscale reconstruction of living brain tissue*, Nature Methods, 20 (2023), pp. 1256–1265.